

Cite this: *Mater. Adv.*, 2020,  
1, 3539Flame spheroidisation of dense and porous  
 $\text{Ca}_2\text{Fe}_2\text{O}_5$  microspheres†Jesús Molinar Díaz,<sup>a</sup> Sabrin Abdus Samad,<sup>a</sup> Elisabeth Steer,<sup>b</sup> Nigel Neate,<sup>bc</sup>  
Hannah Constantin,<sup>c</sup> Md Towhidul Islam,<sup>ad</sup> Paul D Brown<sup>ab</sup> and Ifty Ahmed<sup>\*a</sup>

Compositionally uniform magnetic  $\text{Ca}_2\text{Fe}_2\text{O}_5$  (srebrodolskite) microspheres created via a rapid, single-stage flame spheroidisation (FS) process using magnetite and carbonate based porogen (1:1  $\text{Fe}_3\text{O}_4$ : $\text{CaCO}_3$ ) feedstock powders, are described. Two types of  $\text{Ca}_2\text{Fe}_2\text{O}_5$  microsphere are produced: dense (35–80  $\mu\text{m}$ ), and porous (125–180  $\mu\text{m}$ ). Scanning electron microscopy (SEM) based techniques are used to image and quantify these. Complementary high-temperature X-ray diffraction (HT-XRD) measurements and thermogravimetric analysis (TGA) provide insights into the initial process of porogen feedstock decomposition, prior to the coalescence of molten droplets and spheroidisation, driven by surface tension. Evolution of  $\text{CO}_2$  gas (from porogen decomposition) is attributed to the development of interconnected porosity within the porous microspheres. This occurs during  $\text{Ca}_2\text{Fe}_2\text{O}_5$  rapid cooling and solidification. The facile FS-processing route provides a method for the rapid production of both dense and porous magnetic microspheres, with high levels of compositional uniformity and excellent opportunity for size control. The controllability of these factors make the FS production method useful for a range of healthcare, energy and environmental remediation applications.

Received 3rd August 2020,  
Accepted 13th November 2020

DOI: 10.1039/d0ma00564a

rsc.li/materials-advances

## Introduction

Porous microspheres have been studied extensively for a variety of healthcare and energy applications, ranging from drug-delivery systems and tissue regeneration scaffolds, to batteries and supercapacitors.<sup>1,2</sup> Porous microspheres offer advantageous properties over traditional solid microspheres, with applicability *e.g.* in separation sciences.<sup>3,4</sup> Moreover, for biomedical applications, porous microspheres enable payloads (for drugs, cells, biologics *etc.*) to be incorporated on their surfaces or within the pores. In addition, other physical advantages are recognised, including large specific surface area and low density, along with absorption and release kinetics.<sup>1,5</sup>

The manufacture of porous structures is dependent strongly on the type of material employed. For the case of glass and/or

ceramic scaffolds, methods such as the incorporation of a removable space holder (*via* sintering),<sup>6</sup> polymer foam replication,<sup>7</sup> sol-gel,<sup>8</sup> gel-cast foaming,<sup>9</sup> or solid free-form (3D printing) approaches<sup>10</sup> are typically employed. However, these methods generally involve numerous processing steps which can be time-prolonged and laborious.<sup>2</sup> Residual materials, post thermal dissolution of space holders or sacrificial polymer templates, not only result in contamination of the porous products, but also affect their mechanical and physical properties.<sup>2</sup> In the case of 3D printing, multiple steps are required, such as data acquisition, design/modeling, ink preparation, printing and post-processing treatments (*e.g.* drying and sintering).<sup>11,12</sup> Manufacturing procedures for porous polymer microspheres typically involve emulsion-solvent evaporation, spray drying and phase separation techniques,<sup>1,2,5</sup> whilst ceramic microspheres are processed *via* gelation,<sup>2,5</sup> emulsification or precipitation methods.<sup>1,5</sup> However, when seeking to manufacture microspheres with high levels of interconnected porosity, these methods generally present important limitations relating to scale-up,<sup>5</sup> along with poor control over particle morphology, size and pore size.<sup>2</sup>

Alternatively, the single-stage, flame spheroidisation (FS) process is a unique, fast, cost-effective<sup>5</sup> and promising technique for the large-scale manufacture and simultaneous production of porous and dense microspheres. Feeding irregular shaped particles into a high-temperature flame causes them to melt and form spherical particles upon ejection from the flame,

<sup>a</sup> Advanced Materials Research Group, Faculty of Engineering, University of Nottingham, University Park, Nottingham NG7 2RD, UK.

E-mail: ifty.ahmed@nottingham.ac.uk

<sup>b</sup> Nanoscale and Microscale Research Centre, University of Nottingham, University Park, Nottingham NG7 2RD, UK

<sup>c</sup> Department of Mechanical, Materials and Manufacturing Engineering, Faculty of Engineering, University of Nottingham, University Park, Nottingham NG7 2RD, UK

<sup>d</sup> Department of Applied Chemistry and Chemical Engineering, Faculty of Engineering, Noakhali Science and Technology University, Noakhali 3814, Bangladesh

† Electronic supplementary information (ESI) available. See DOI: 10.1039/d0ma00564a

mediated by surface tension followed by rapid cooling.<sup>13</sup> This process has recently been developed and reported for glass porous microspheres.<sup>2,14</sup> However, this is the first report on the production of porous and dense microsphere from ceramics (*i.e.* magnetite) using the FS process.

Magnetic microparticles (MMP) have great potential in healthcare and pharmaceutical applications, and for environmental remediation. In particular, magnetic microspheres (MMS) are considered advantageous for biomedical applications due to their chemical stability,<sup>15</sup> biocompatibility<sup>15,16</sup> and ease of transport within blood vessels, if they can be produced at a size (<3 μm) suitable for flow inside hepatic arteries.<sup>17</sup> Magnetite (Fe<sub>3</sub>O<sub>4</sub>) microspheres and nanospheres have been investigated for magnetic-induced hyperthermia treatment of cancers<sup>18</sup> and have been employed successfully as contrast agents in magnetic resonance imaging (MRI),<sup>15,19</sup> whilst targeted magnetic drug-delivery systems are currently at the pre-clinical stage.<sup>15</sup> MMP have also proved beneficial for environmental remediation, including the removal of heavy metals and radionuclides from contaminated soil and water, and phosphates from wastewater,<sup>15,20</sup> along with oils and chemicals/toxins from the environment.<sup>20</sup>

Here, we demonstrate (for the first time) a novel application of the FS process, using Fe<sub>3</sub>O<sub>4</sub> powder/CaCO<sub>3</sub> porogen combinations, to create mixtures of compositionally uniform, porous and dense, magnetic Ca<sub>2</sub>Fe<sub>2</sub>O<sub>5</sub> microspheres, with potential for a range of biomedical and environmental remediation applications.

## Experimental

### Materials and methods

The starting materials comprised as-supplied powders of iron(II,III) oxide (Fe<sub>3</sub>O<sub>4</sub>; <5 μm, 95%) (Sigma-Aldrich, UK) and calcium carbonate porogen (CaCO<sub>3</sub>, 98%) (Fisher Scientific UK Ltd). 5 mg of Fe<sub>3</sub>O<sub>4</sub> and 5 mg of CaCO<sub>3</sub> (1:1 ratio), combined with droplets of 2% aqueous solution poly vinyl alcohol (PVA; Sigma-Aldrich, UK) to act as binder, were mixed using a mortar and pestle and dried at 37 °C for 24 h (see ESI†). The powders prepared were flame-spray processed using a thermal spray gun (MK74, Metallization Ltd, UK) coupled with oxy-acetylene (O<sub>2</sub>/C<sub>2</sub>H<sub>2</sub>; 1:1 gas flow ratio). The microsphere products exiting the flame were collected using glass trays, positioned a short distance away from the thermal spray gun, and stored in glass vials for characterisation.

## Materials characterisation

Structural characterisation of the FS products was performed using X-ray diffraction (XRD) (Bruker D8 Advance with Da Vinci using a LYNXEYE XE-T detector in 1D mode; Cu Kα radiation (λ = 0.15406 nm); 40 kV and 40 mA; step size 0.02°; step time 0.2 s; total time/step 29.8 s; 21 °C).

Topographic imaging was performed using scanning electron microscopy (SEM) (FEI XL30; 5kV; spot size 2.5; 13.3 mm working distance, secondary electron (SE) imaging mode).

Microsphere and pore size distributions were established using ImageJ 1.51h software (National Institutes of Health, USA). Complementary backscattered electron (BSE) imaging and chemical analysis of sieved and sectioned microspheres was performed using SEM-based mineral liberation analysis (MLA) (FEI Quanta600 MLA, 20 kV; spot size 7) equipped with energy dispersive X-ray spectroscopy (EDS) and computer software (FEI Quanta600 MLA, Bruker/JKTech/FEI software), used for elemental composition analysis and data acquisition for automated mineralogy. A Test sieve (stainless steel frame; 203 × 50 mm; 32 μm mesh; VWR International) was used to filter out particles sized below 32 μm. Sectioned samples were obtained by embedding the sieved microspheres in cold epoxy resin, followed by sequential mechanical grinding and polishing using silicon carbide discs and diamond cloths, respectively. Polished samples were cleaned and dried before being carbon coated.<sup>2</sup>

Complementary thermogravimetric analysis (TGA) (SDT Q600; 40–1500 °C; heating rate 10 °C min<sup>-1</sup>; air) and high-temperature XRD (HT-XRD) (Bruker D8 Advance Series 2 with MRI TC-Basic temperature chamber; Cu Kα radiation (λ = 0.15406 nm); step size 0.050°; step time 2 s; temperatures: 30, 450, 550, 650, 750, 950 and 1050 °C; heating rate 10 °C min<sup>-1</sup>) were used to investigate Fe<sub>3</sub>O<sub>4</sub>:CaCO<sub>3</sub> mixed powders, as a function of heating. Semi-quantitative analysis (Bruker DIFFRAC.EVA software) was used to determine weight fractions of the constituent products.

## Results

### Structural characterisation

Fig. 1 presents an XRD pattern for 1:1 Fe<sub>3</sub>O<sub>4</sub>:CaCO<sub>3</sub> FS-processed products (unsieved), confirming the presence of Ca<sub>2</sub>Fe<sub>2</sub>O<sub>5</sub> (srebrodolskite) (ICDD PDF no. 00-047-1744), Fe<sub>3</sub>O<sub>4</sub> (magnetite) (ICDD PDF no. 01-087-0244), Fe<sub>2</sub>O<sub>3</sub> (ICDD PDF 00-033-0664) and CaCO<sub>3</sub> (calcite) (ICDD PDF no. 00-047-1743).

### Microsphere morphologies

Fig. 2a presents a low magnification SE image of these FS Fe<sub>3</sub>O<sub>4</sub>:CaCO<sub>3</sub> products, demonstrating a mixture of large porous (125–180 μm) and smaller dense (35–80 μm) microspheres, along with some small irregular-shaped particles. A total of 124 pores measured from five different porous microspheres showed a minimum and maximum size of 1.8 and 64.5 μm, respectively, with a mean pore size of 13.1 μm (SD of 12.6 μm). Fig. 2b shows a typical spheroidised porous microsphere in detail, whilst with

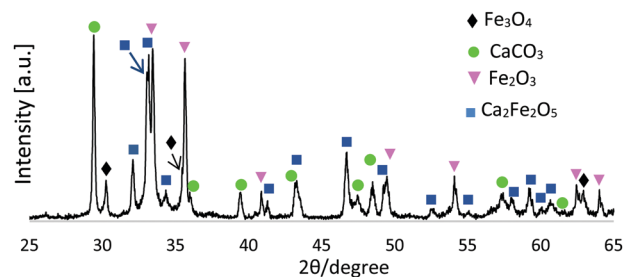


Fig. 1 XRD pattern for FS-processed Fe<sub>3</sub>O<sub>4</sub>:CaCO<sub>3</sub>.





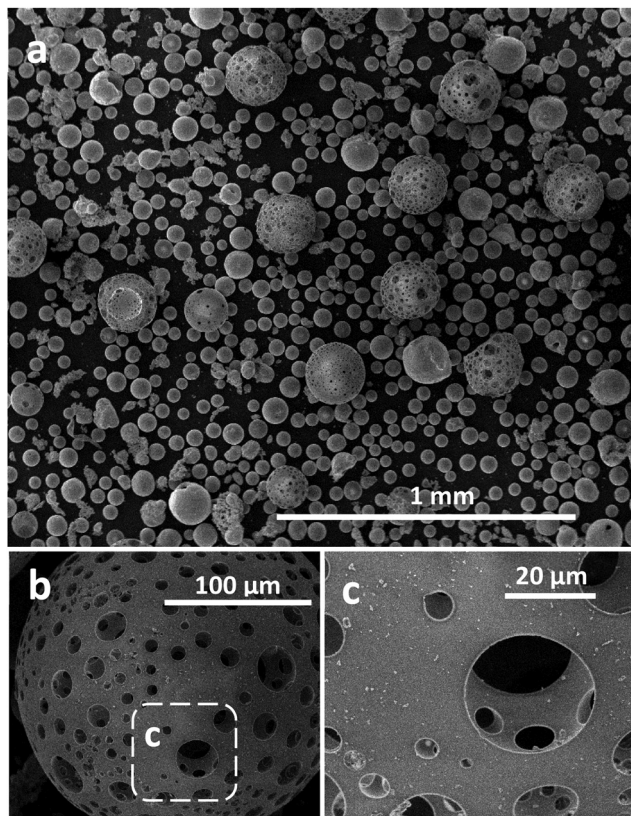


Fig. 2 SE images of FS-processed  $\text{Fe}_3\text{O}_4:\text{CaCO}_3$  showing: (a) small, dense and large, porous microspheres; (b) details of a porous microsphere; and (c) microsphere interconnected porosity (boxed in region (b)).

the magnified boxed region of Fig. 2c demonstrates the interconnected porous microstructure. Placing a simple bar magnet next to this FS-processed sample, following sieving, confirmed that the microsphere products remained magnetic post processing (see ESI†).

### Compositional analysis

Fig. 3a presents a BSE image of a sieved, resin embedded and sectioned sample, comprising a mixture of the porous and dense microsphere products. A variety of developed porosities and very high levels of interconnected porosity for the larger microspheres is evident. Interestingly, mineral mapping analysis (Fig. 3b) provided evidence for the highly homogenous distribution of  $\text{Ca}_2\text{Fe}_2\text{O}_5$  throughout both dense and porous microspheres. A total of 1501 particles (99.75 wt% of the sample) were classified as srebrodolskite by the MLA software whilst using a standard 70% matching threshold (see ESI†). In addition, EDS analysis showed the elemental composition to be consistent with srebrodolskite, *i.e.* Ca – 19.1%, Fe – 57%, O – 23.9%.

### Thermal analysis and structural transformation

Complementary TGA was used to profile the wt% change of the starting  $\text{Fe}_3\text{O}_4:\text{CaCO}_3$  powder mix (non-spheroidised starting powders), as a function of increasing temperature. The TGA curve of Fig. 4 demonstrated an initial 2.5 wt% increment from 40 °C to 611 °C, consistent with the oxidation of  $\text{Fe}_3\text{O}_4$  to  $\text{Fe}_2\text{O}_3$ ,<sup>21</sup> followed by a drop of 11 wt%, from 611 °C to 712 °C, attributable to the decomposition of  $\text{CaCO}_3$ <sup>22</sup> porogen within the sample.

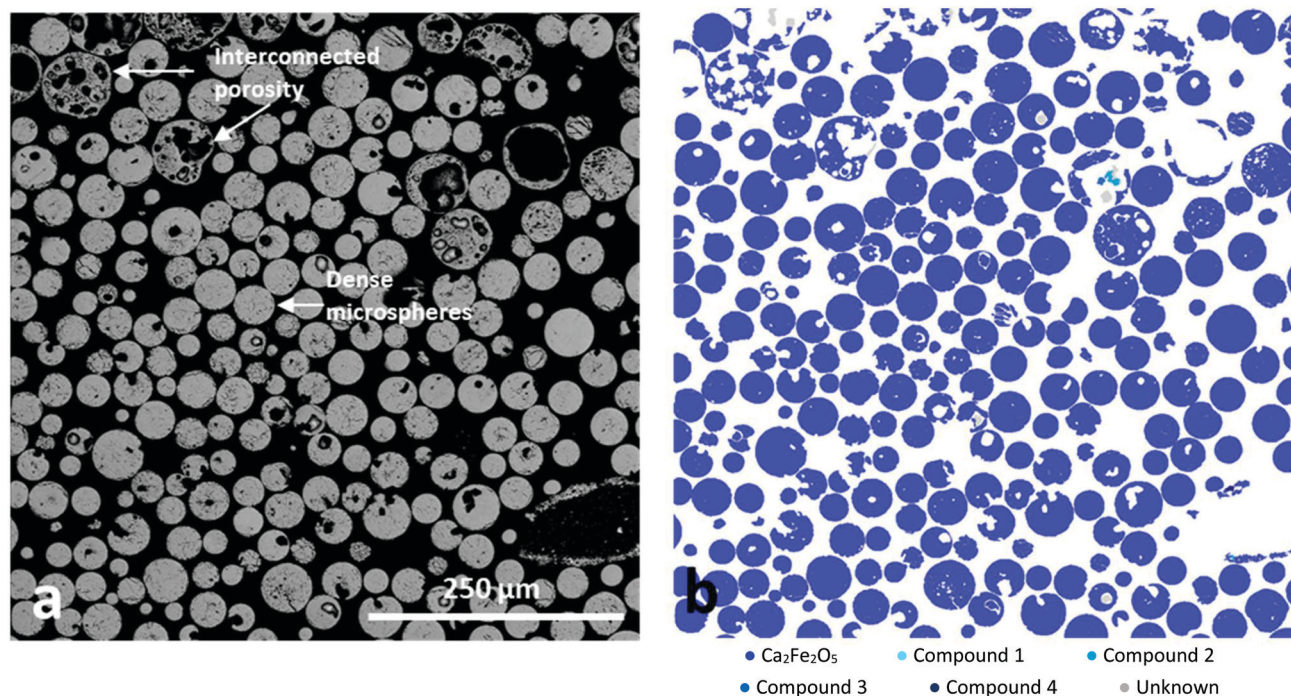


Fig. 3 (a) BSE image and (b) MLA compositional analysis of FS-processed  $\text{Fe}_3\text{O}_4:\text{CaCO}_3$ , following sieving and sectioning, illustrating microsphere porosity and demonstrating very high levels of  $\text{Ca}_2\text{Fe}_2\text{O}_5$  (blue) compositional homogeneity. Phases definitions are in the ESI.†



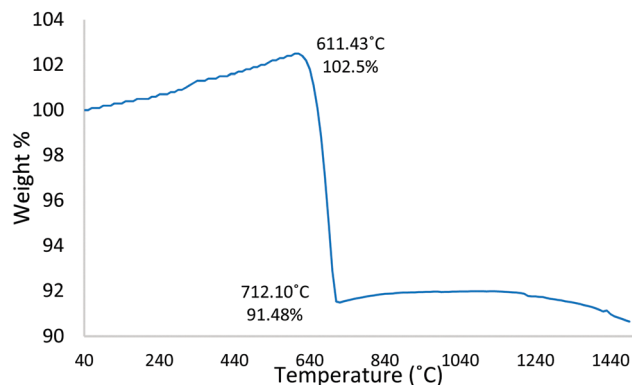


Fig. 4 T-wt% curve for  $\text{Fe}_3\text{O}_4\text{:CaCO}_3$ .

Further, HT-XRD investigations were performed to profile the structural transformation of the powder mix as a function of slowly increasing temperature ( $10^\circ\text{C min}^{-1}$ ), providing insight into the chemical reaction pathway. Overall, the evidence demonstrated a progressive transformation of  $\text{Fe}_3\text{O}_4\text{:CaCO}_3$  to a mixture of  $\text{CaCO}_3$ ,  $\text{Fe}_2\text{O}_3$  and  $\text{Ca}_2\text{Fe}_2\text{O}_5$  (Fig. 5), distinct from the  $\text{CaCO}_3$ ,  $\text{Fe}_3\text{O}_4$  and  $\text{Ca}_2\text{Fe}_2\text{O}_5$  products for the case of rapidly-processed FS samples (Fig. 1). Fig. 5a confirmed the starting powder to be a mixture of magnetite and calcite ( $\text{CaCO}_3$ ), whilst their defining crystalline peaks progressively diminished with increasing temperature up to  $550^\circ\text{C}$  (Fig. 5c, black arrows). A small peak attributable to the onset of  $\text{Fe}_2\text{O}_3$  formation emerged at  $450^\circ\text{C}$  (Fig. 5b, pink arrow). At  $650^\circ\text{C}$  and  $750^\circ\text{C}$  more intense and sharper peaks indicative of the development of  $\text{Ca}_2\text{Fe}_2\text{O}_5$  became evident (Fig. 5d and e blue arrows). A summary of the constituent products, as a function of temperature, is given in Table 1 (whilst noting the possibility of systematic error affecting the absolute values).

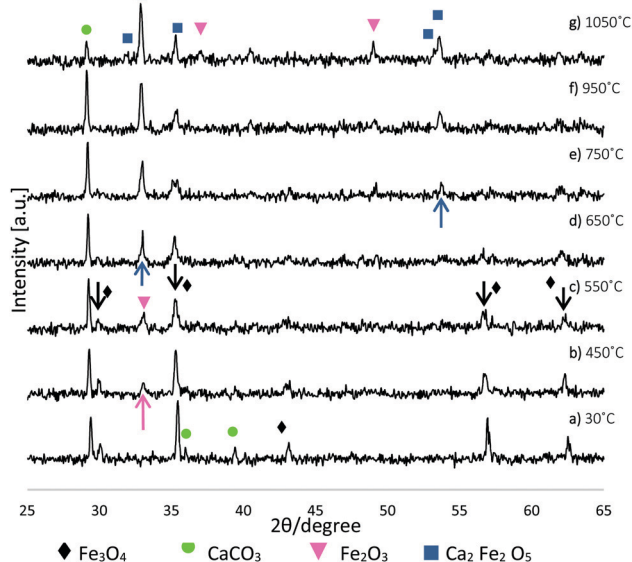


Fig. 5 XRD patterns illustrating  $\text{Fe}_3\text{O}_4\text{:CaCO}_3$  structural transformation as a function of increasing temperature.

Table 1 Wt% constituents of mixed  $\text{Fe}_3\text{O}_4\text{:CaCO}_3$  powder with increasing temperature

	30 °C	450 °C	550 °C	650 °C	750 °C	950 °C	1050 °C
$\text{Fe}_3\text{O}_4$	30.2	11.9	11	6.1	—	—	—
$\text{CaCO}_3$	69.8	61.5	74.6	41.1	43.7	41.2	14.4
$\text{Fe}_2\text{O}_3$	—	26.6	14.4	20.4	21.7	26.2	38.1
$\text{Ca}_2\text{Fe}_2\text{O}_5$	—	—	—	32.5	34.6	32.6	47.4

## Discussion

This first report of the application of the rapid, single-stage, FS-processing method to magnetite demonstrates the transformation of  $\text{Fe}_3\text{O}_4\text{:CaCO}_3$  to a mixture of dense and highly porous  $\text{Ca}_2\text{Fe}_2\text{O}_5$  magnetic microspheres (with smaller, unreacted particles of  $\text{Fe}_3\text{O}_4$ ,  $\text{CaCO}_3$  and reacted  $\text{Fe}_2\text{O}_3$  removed simply by sieving). Fig. 6 schematically presents the key stages of dynamic evolution proposed for these FS-processed powders.

The prepared  $\text{Fe}_3\text{O}_4\text{:CaCO}_3$  particles were fed into the high-temperature flame ( $\sim 3100^\circ\text{C}$ ) where rapid melting and some droplet coalescence occurred. The molten particles acquired spherical shape post exiting the flame due to surface tension. The development of compositionally uniform, dense and porous  $\text{Ca}_2\text{Fe}_2\text{O}_5$  microspheres, upon rapid cooling and solidification, is consistent with the  $\text{CaO}:\text{Fe}_2\text{O}_3$  (2:1 molar ratio) section of  $\text{Ca-Fe-O}$  phase diagram.<sup>23</sup> It is considered that  $\text{CO}_2$ , produced during  $\text{CaCO}_3$  decomposition and trapped in the form of gas bubbles within the molten droplets, rapidly escaped at the point of solidification and hence was responsible for the production of the larger  $\text{Ca}_2\text{Fe}_2\text{O}_5$  microspheres exhibiting high levels of interconnected porosity (Fig. 2b and c). The high compositional uniformity of the microspheres (Fig. 3b) confirmed that product composition was established before porosity development.

The evidence from HT-XRD and TGA investigations, both acquired under conditions of slow heating rate ( $10^\circ\text{C min}^{-1}$ ), provided complementary information relating to particle decomposition and reaction pathways. The HT-XRD data (Fig. 5 and Table 1) showed a transition of magnetite to hematite between  $30^\circ\text{C}$  and  $650^\circ\text{C}$ , whilst TGA data (Fig. 4) showing 2.5% weight increment between  $40$ – $611^\circ\text{C}$  was also consistent with an initial stage of  $\text{Fe}_3\text{O}_4$  oxidation (eqn (1)). The TGA curve also showed substantial weight loss of 11% between  $611$ – $712^\circ\text{C}$ , consistent with the decomposition of  $\text{CaCO}_3$  porogen to  $\text{CaO}$  and  $\text{CO}_2$  evolution (eqn (2)). Indeed, it is noted that  $\text{Ca}_2\text{Fe}_2\text{O}_5$  brownmillerite-type phase (srebrodolskite) formation can occur as a consequence of  $\text{Fe}_2\text{O}_3$  and  $\text{CaO}$  reaction (eqn (3)), whilst the formation of mineral srebrodolskite is in agreement with previous work on  $\text{CaO}:\text{Fe}_2\text{O}_3$  thermal processing.<sup>22,24</sup> In particular, Boyanov,<sup>24</sup> reporting on the formation of calcium ferrites ( $\text{Ca}_2\text{Fe}_2\text{O}_5$  and  $\text{CaFe}_2\text{O}_4$ ) in the range of  $900$ – $1200^\circ\text{C}$ , investigated by HT-XRD, noted complete consumption of  $\text{CaO}:\text{Fe}_2\text{O}_3$  by  $1200^\circ\text{C}$ . This balance helps to explain the presence of residual  $\text{Fe}_2\text{O}_3$  peaks at  $1050^\circ\text{C}$  in Fig. 5g. The absence of  $\text{CaO}$  peaks in Fig. 5 is attributed to the immediate reaction occurring between  $\text{Fe}_2\text{O}_3$  and  $\text{CaO}$  once  $\text{CaCO}_3$  is decomposed (eqn (3)). Fig. 5 also showed that from  $750^\circ\text{C}$ ,





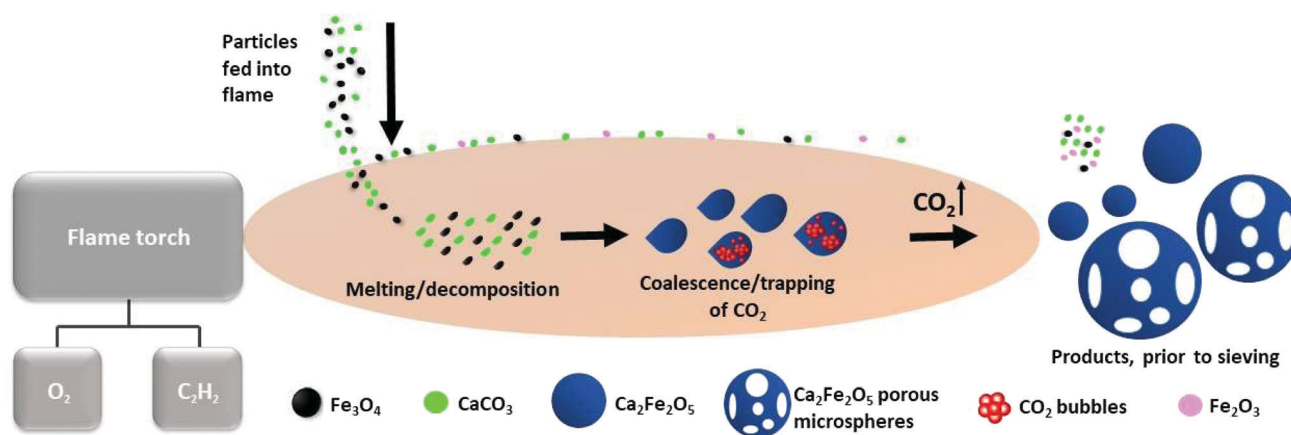
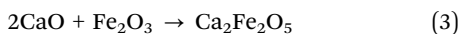
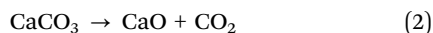
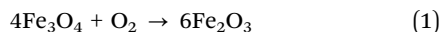


Fig. 6 Schematic representation of dense and porous  $Ca_2Fe_2O_5$  microsphere formation, via oxy-acetylene FS processing.

$Ca_2Fe_2O_5$  peaks gradually become more intense, evidencing srebrodolskite formation, whereas  $CaCO_3$  peaks become less intense. Table 1 records a significant 26.8% loss of weight of  $CaCO_3$  from 950 °C (41.2%) to 1050 °C (14.4%).



Conversely, XRD peaks attributable to  $Fe_3O_4$  and  $CaCO_3$  in Fig. 1 were attributed to small particles of unmelted magnetite and porogen, with the suggestion that these particles were pushed to the periphery and coldest part of the flame, either elevated by the oxy-acetylene gas-pressure (Fig. 6), or due to collision with other particles. Similarly,  $Fe_2O_3$  XRD peaks identified within the FS reaction products (Fig. 1) reflect a reacted portion of  $Fe_3O_4$  that was also pushed to the periphery of the flame. It is suggested that the temperature at the periphery of the flame was sufficient to oxidise small particles of magnetite. An FS generated melt composed of  $CaO:Fe_2O_3$  (2:1 molar ratio) is consistent with the formation of  $Ca_2Fe_2O_5$  upon rapid droplet cooling.

The magnetic expression of the FS-processed  $Ca_2Fe_2O_5$  microsphere products was attributed to their structural arrangements, comprising ordered oxygen vacancies with alternating layers of corner-sharing  $FeO_4$  tetrahedra and  $FeO_6$  octahedra.<sup>25,26</sup> This structure provides for two types of magnetic moment, arising from  $FeO_4$  and  $FeO_6$ ,<sup>27</sup> corresponding to antiferromagnetic and weak ferromagnetic behaviour, respectively.<sup>26,27</sup>

It is noted that manufactured, uniform  $Ca_2Fe_2O_5$  microspheres have relevance in a number of different fields, including biomedical, energy and environmental remediation. Further, developed porous microspheres provide the opportunity to incorporate and deliver active species to a specific location or environment, with potential applications ranging from environmental remediation, and industrial waste-water purification agents in particular, to energy stores and supercapacitors.<sup>28</sup> Alternatively, given their spherical-shape, porous morphology and ferromagnetic expression,  $Ca_2Fe_2O_5$

microspheres could also be exploited for healthcare applications, e.g. MRI<sup>15,19</sup> and drug-delivery systems.<sup>29</sup>

## Conclusions

Dense (small, 35–80  $\mu m$ ) and porous (large, 125–180  $\mu m$ )  $Ca_2Fe_2O_5$  (srebrodolskite) magnetic microspheres, with very high levels of compositional uniformity, have been produced via a facile, rapid, single-stage, flame spheroidisation process. Direct evidence from XRD, SEM and MLA characterisation, along with complementary HT-XRD and TGA investigations, have allowed a mechanism to be established, describing the morphological development of  $Ca_2Fe_2O_5$  microspheres from starting 1:1  $Fe_3O_4:CaCO_3$  feedstock powder. It is proposed that the evolution of  $CO_2$  gas bubbles (arising from decomposition of the  $CaCO_3$  porogen), trapped within coalescing molten droplets, was responsible for the development of interconnected porosity during  $Ca_2Fe_2O_5$  cooling and rapid solidification. The combination of compositional control and high levels of porosity achieved opens up new opportunities, to explore the application of magnetic microspheres for a range of biomedical, energy and environmental remediation challenges.

## Conflicts of interest

There are no conflicts to declare.

## Acknowledgements

Jesús Molinar Díaz would like thank the CONACyT programme and the Faculty of Engineering, University of Nottingham, for funding this work. With thanks also to Martin Roe and Julie Watts at the Nanoscale and Microscale Research Centre (nmRC), University of Nottingham, for training on SEM facilities and ImageJ software; and Jason Greaves from the Faculty of Engineering, University of Nottingham, for complementary TGA training.



## References

- 1 Y. Cai, Y. Chen, X. Hong, Z. Liu and W. Yuan, *Int. J. Nanomed.*, 2013, **8**, 1111–1120.
- 2 K. M. Z. Hossain, U. Patel, A. R. Kennedy, L. Macri-Pellizzeri, V. Sottile, D. M. Grant, B. E. Scammell and I. Ahmed, *Acta Biomater.*, 2018, **72**, 396–406.
- 3 A. Ahmed, K. Skinley, S. Herodotou and H. Zhang, *J. Sep. Sci.*, 2018, **41**, 99–124.
- 4 W. Li and J. Y. Walz, *Sci. Rep.*, 2014, **4**, 4418.
- 5 K. M. Z. Hossain, U. Patel and I. Ahmed, *Prog. Biomater.*, 2015, **4**, 1–19.
- 6 B. Arifvianto and J. Zhou, *Materials*, 2014, **7**, 3588–3622.
- 7 M. A. A. Muhamad Nor, L. C. Hong, Z. Arifin Ahmad and H. Md Akil, *J. Mater. Process. Technol.*, 2008, **207**, 235–239.
- 8 H. Cai, W. Mu, W. Liu, X. Zhang and Y. Deng, *Inorg. Chem. Commun.*, 2015, **51**, 71–74.
- 9 S. Hooshmand, J. Nordin and F. Akhtar, *Int. J. Ceram. Eng. Sci.*, 2019, **1**, 77–84.
- 10 Y. J. Tan, X. Tan, W. Y. Yeong and S. B. Tor, *Sci. Rep.*, 2016, **6**, 39140.
- 11 C. Minas, D. Carnelli, E. Tervoort and A. R. Studart, *Adv. Mater.*, 2016, **28**, 9993–9999.
- 12 L. Alison, S. Menasce, F. Bouville, E. Tervoort, I. Mattich, A. Ofner and A. R. Studart, *Sci. Rep.*, 2019, **9**, 409.
- 13 D. Gupta, K. M. Z. Hossain, I. Ahmed, V. Sottile and D. M. Grant, *ACS Appl. Mater. Interfaces*, 2018, **10**, 25972–25982.
- 14 D. Gupta, K. M. Z. Hossain, I. Ahmed, V. Sottile and D. M. Grant, *ACS Appl. Mater. Interfaces*, 2018, **10**, 25972–25982.
- 15 D. Xiao, T. Lu, R. Zeng and Y. Bi, *Microchim. Acta*, 2016, **183**, 2655–2675.
- 16 A. Rafieepour, M. R. Azari, H. Peirovi, F. Khodaghali, J. P. Jaktaji, Y. Mehrabi, P. Naserzadeh and Y. Mohammadian, *Toxicol. Ind. Health*, 2019, **35**, 703–713.
- 17 N. Li, F. Michaud, Z. Nosrati, D. Loghin, C. Tremblay, R. Plantefevre, K. Saatchi, U. O. Hafeli, S. Martel and G. Soulez, *IEEE Trans. Biomed. Eng.*, 2019, **66**, 2331–2340.
- 18 M. V. Velasco, M. T. Souza, M. C. Crovace, A. J. A. D. Oliveira and E. D. Zanotto, *Biomed. Glasses*, 2019, **5**, 148.
- 19 A. K. Fahlvik, E. Holtz and J. Klaveness, *Magn. Reson. Imaging*, 1990, **8**, 363–369.
- 20 J. D. Orbell, H. V. Dao, L. N. Ngeh and S. W. Bigger, *Environmentalist*, 2007, **27**, 175–182.
- 21 E. R. Monazam, R. W. Breault and R. Siriwardane, *Ind. Eng. Chem. Res.*, 2014, **53**, 13320–13328.
- 22 T. Beuvier, J. F. Bardeau, B. Calvignac, G. Corbel, F. Hindré, J.-M. Greneche, F. Boury and A. Gibaud, *J. Raman Spectrosc.*, 2013, **44**, 489–495.
- 23 T. Hidayat, D. Shishin, S. Decterov and E. Jak, *Metall. Mater. Trans. B*, 2015, **47**, 256–281.
- 24 B. Boyanov, *J. Min. Metall., Sect. B.*, 2005, **41**, 67–77.
- 25 T. L. Phan, P. T. Tho, N. Tran, D. H. Kim, B. W. Lee, D. S. Yang, D. V. Thiet and S. L. Cho, *J. Electron. Mater.*, 2018, **47**, 188–195.
- 26 B. F. Amorim, M. A. Morales, F. Bohn, A. S. Carriço, S. N. de Medeiros and A. L. Dantas, *Phys. B*, 2016, **488**, 43–48.
- 27 I. Kagomiya, Y. Hirota, K. I. Kakimoto, K. Fujii, M. Shiraiwa, M. Yashima, A. Fuwa and S. Nakamura, *Phys. Chem. Chem. Phys.*, 2017, **19**, 31194–31201.
- 28 D. S. Vavilapalli, S. Banik, R. G. Peri, K. Muthuraaman, M. Miryala, M. Murakami, K. Alicja, K. Asokan, M. S. Ramachandra Rao and S. Singh, *Sci. Rep.*, 2020, **10**, 2713.
- 29 K. El-Boubbou, R. Ali, H. Al-Zahrani, T. Trivilegio, A. H. Alanazi, A. L. Khan, M. Boudjelal and A. AlKushi, *Sci. Rep.*, 2019, **9**, 9481.

